Cassava peel derived self-doped and hierarchical porous carbon as an optimized electrode for the ultra-high energy density of supercapacitor

by Rika Taslim

Submission date: 12-Apr-2023 05:48PM (UTC+0700)
Submission ID: 2062432183
File name: 8._Diamond_Related_Material_2022_Ubi_kayu.pdf (2.62M)
Word count: 10449
Character count: 56974

Diamond & Related Materials 129 (2022) 109407

Contents lists available at ScienceDirect

Diamond & Related Materials

journal homepage: www.elsevier.com/locate/diamond

Cassava peel derived self-doped and hierarchical porous carbon as an optimized electrode for the ultra-high energy density of supercapacitor

Eva Wahyuni Harahap [a], Erman Taer [a,*], Ari Sulistyo Rini [a], Rika Taslim [b], Apriwandi Apriwandi [a]

[a] Department of Physics, Faculty of Mathematics and Natural Sciences, University of Riau, Pekanbaru, Riau 28293, Indonesia
[b] Department of Industrial Engineering, State Islamic University of Sultan Syarif Kasim Riau, Pekanbaru, Riau 28293, Indonesia

ARTICLE INFO

Keywords:
Cassava peel
Hierarchical porous carbon
Electrode material
Energy density
Supercapacitor

ABSTRACT

The development of advanced electrode materials with optimized properties, including structural morphology, high porosity, and functional group doping, is very important to enhance the energy density of solid-state supercapacitors. Here, a hierarchical 3D porous carbon self-doping obtained from cassava peel through an environmentally benign approach to optimize the supercapacitor working electrode material. The unique sponge-like interconnected pore structure and self-doping features are controlled through chemical impregnation (CIP) of $ZnCl_2$ (CIP/Z), KOH (CIP/K), and H_3PO_4 (CIP/H) and high-temperature pyrolysis in an N_2&CO_2 gaseous environment. Furthermore, the optimized CIP/Z carbon material exhibits high content of 94.606 % and a self-doping oxygen heteroatom of about 2.672 %. The unique sponge-like morphology possessed enriches micropores of 94 %, indicating high performance as an electrode material. The electrochemical properties were assessed through a symmetric supercapacitor system assembled in a solid free-binding coin yielding an excellent specific capacitance of 257 F g^{-1} at 1 A g^{-1}. Meanwhile, the optimized electrode has a high rate capability of 92.43 % and maintained a coulombic efficiency of up to 91.10 % at 10 A g^{-1}. The best working efficiency supercapacitor cell can show a jump in energy density of 35.69 Wh kg^{-1} at a specific power of 167.68 W kg^{-1} in an aqueous electrolyte of 1 M H_2SO_4. These excellent results provide important insights for optimizing electrode materials derived from cassava peel-based porous carbon for symmetrically designed supercapacitors of binder-free solid coins in aqueous electrolytes with high energy density.

1. Introduction

The slow transformation of the world's clean and renewable energy sources and the continuous burning of fossil fuels are driving increasingly massive environmental issues [1]. Extreme climate change, rising sea levels, increasing air pollution, and high carbon dioxide emissions are major environmental problems. They are a global conversation and a top focus issue in intellectual studies and technological research [2,3]. Great efforts and effective solutions continue to be proposed in formal and informal institutions to accelerate the transit of fossil fuel-free industrial technologies and optimize renewable energy resources. The continued development of these technologies requires superior energy storage devices with high efficiency and extraordinary energy and power density [4]. Several high-performance energy storage devices have been reported, such as fuel cells, batteries, and supercapacitors [5,6]. Unlike fuel cells and batteries, whose charge performance is controlled by electrochemical reaction kinetics, which limits their life cycle, supercapacitors are achieved through interfacial charge transfer, providing high energy and power density and enabling infinite life cycle stability [7,8]. Therefore, the supercapacitor can effectively find many possible applications as a power source in special operations and in adjusting intermittent energy flows [9,10].

Supercapacitor devices have been commercially available with specifications of specific energy in the range of 5–15 Wh kg^{-1} and power density at >10,000 W kg^{-1} [11,12]. The unbalanced low energy density limits the application of advanced technology despite its high specific power. In addition, the high cost of raw materials and complicated electrode fabrication are further challenges. The specific energy of supercapacitors can be increased through modification of the electrode material properties by presenting high surface area [13], 2D nanostructures [14], 3D hierarchical pore morphology [15], and multi-doping heteroatom effects [16]. One of the electrode materials with a

* Corresponding author.
E-mail address: erman.taer@lecturer.unri.ac.id (E. Taer).

https://doi.org/10.1016/j.diamond.2022.109407
Received 25 July 2022; Received in revised form 21 September 2022; Accepted 26 September 2022
Available online 28 September 2022

2-3D morphology is graphene and conduction polymer, which can produce a high specific surface area of around 3000–4000 $m^2\ g^{-1}$ and optimized pore framework construction with tremendous potential for doping heteroatom functional groups [17,18]. In addition, their excellent conductivity, mechanical strength, and flexibility make them applicable to supercapacitor energy storage devices of combined type EDLC and pseudocapacitance, which exhibit superior electrochemical power and energy [19–21]. This combination of outstanding material properties can deliver nearly 10 times the energy density of commercial devices with maintained power density. However, graphene and polymer materials cannot reduce their fabrication complexity and source-based weakness because they are often derived from non-renewable raw materials. These include graphite, coal, fossil remains, and synthetic materials through complex procedures with hazardous, corrosive, toxic and mechanical peeling that consumes energy. Obtaining an abundant, inexpensive, renewable source of electrode base material and a zero pollution synthesis process while optimizing material properties, including diverse pore distribution, high specific surface area, and wettability properties for increased high energy density, is necessary to increase productivity and enable the use on advanced technology.

Previously, biomass-based carbon has shown tremendous potential as a source of sustainable electrode materials with competitive electrochemical and material properties. Apart from their abundant, renewable, and inexpensive source material, carbon materials are obtained through an easy process with optimized material properties, including high surface area up to 4100 $m^2\ g^{-1}$, excellent adsorption capacity, high porosity, and presence of surface functional groups, thermal stability, and good kinetics [22–24]. Biomass-based carbon materials are derived from glucose, hemicellulose, lignin, and cellulose from plant materials, grass, wood, agricultural waste, organic production house waste, and animal residues treated by carbonization, hydrothermal energy, chemical impregnation, and activation [25,26]. Compared with metal oxides, graphene, and conduction polymers, activated carbon has higher cyclic stability with almost zero by-products, although it has a fairly high internal resistance (Rct). For example, activated carbon from a hysterophorous leaf of Parthenium derivative (biomass) highlights that an ultrahigh surface area of 4104 $m^2\ g^{-1}$ with a rich micropores structure significantly affects device performance [22]. An extraordinary specific surface area is required for maximum double layer formation, great cyclic stability of supercapacitors, and facile removal of emerging pollutants. Wang et al. 2020 found that pine wood biomass is a strong candidate for synthesizing carbon nanofibers for binder-free flexible electrode materials through electrospinning [27]. Furthermore, CNFs prepared with 30 % bioliquid from pine wood and 70 % polyacrylonitrile have a high specific surface area and enrich microporous, which is the key to its electrochemical performance with a specific capacitance of 349 $F\ g^{-1}$ at 0.5 $A\ g^{-1}$. High mesoporous hierarchical porous carbon based on cornstalk pith exhibits significant specific energy of 46 $Wh\ kg^{-1}$ when used as a coin-type symmetric supercapacitor [28]. Energy storage devices can be vastly improved with the application of optimization. A similar analysis was also conducted on the porous activated carbon derived from the biomass of watermelon [29], sakura [30]. Gopalakrishnan et al. (2020) studied the capacitance of carbon electrodes consisting of one to four doped heteroatoms to enhance the electrochemistry of supercapacitors through a combination of electric double-layer and pseudocapacitance effects [31]. The wettability and faradaic redox reactions obtained from heteroatoms increase the capacitive properties of the electrode material. In addition, carbonaceous materials are usually doped with various electrochemically active functional groups, which exhibit apparent capacitance [16,32]. However, biomass-derived activated carbon often lacks nanostructure, high specific surface area, hierarchical morphology, and concurrent heteroatom doping. The synthesis obtained by a feasible and low-cost approach is still a challenge.

This study reports a hierarchical porous activated carbon derived from cassava peels through an up-to-date, easy, and pollution-free approach. It has been reported that cassava peel contains high chemical compounds cellulose of 37.0–66.9 % and lignin of 11.3–37.9 % [33]. These two compounds contribute to providing micro and meso structures which important for ion diffusion and carbon storage [34]. Previous studies have reported cassava peel-derived activated carbon as a supercapacitor electrode [35–37]. However, its porosity and morphological structure have not been fully optimized, which affects the relatively low electrochemical performance. The synthesis technique involves still synthetic materials inhibiting the device's novelty. A cassava peel-derived activated carbon was offered with a hierarchical pore structure and heteroatom self-doping through an up-to-date, easy, pollution-free approach. The precursor's hierarchical pore and 3D morphology were optimized by chemical impregnation of $ZnCl_2$, KOH, and H_3PO_4, followed by high-temperature pyrolysis. In addition, the porous carbon is designed as a binder-free coin to maintain the high conductivity of the base material. In a two-electrode configuration system in a binder-free solid coin design, the optimized sample exhibits a high specific capacitance of 257 $F\ g^{-1}$ at 1 $A\ g^{-1}$ in 1 M H_2SO_4. The performance of optimized supercapacitor devices was effectively discussed with the rate capability of the Ragone plot and capacitance retention. Lastly, this study presents an ingenious design for preparing hierarchical porous carbon based on the useful microstructure of cassava peel.

2. Materials and methods

2.1. Materials

Cassava peel, as the main precursor, is prepared from the plantations of the Pekanbaru community activity unit. Chemical activator agents KOH, $ZnCl_2$, and H_3PO_4, were obtained from EMSURE®, Merck KGaA with Cas-No: 1310-58-3, Cas-No: 7646-85-7, and Ph Eur ACS, ISO, Reag K5202373, respectively. The N_2 and CO_2 gases are supplied from PT. SAMATOR Aneka Gas Industri Tbk. Meanwhile, Duck eggshell membranes were prepared as an organic separator to prepare two electrodes.

2.2. Preparation of cassava peel precursor powder

Cassava peels were harvested from the plantations of the Pekanbaru community activity unit and washed in a water container for several cycles until dirt, soil, and sand had been completely removed. After cleaning, they were cut into small pieces, followed by drying at 110 °C for 48 h. Subsequently, the dried precursors were pre-carbonized in a vacuum oven from 50 to 250 °C with the oven heating rate at 2 °C/min. The solid brittle product was crushed to obtain the cassava peel powder precursor. The powder obtained was homogenized through a 250 mesh sieving. The final result obtained pre-carbonized cassava peel powder precursor with dark brown physical color.

2.3. Preparation of solid activated carbon based on cassava peel waste

A series of solid activated carbon materials were prepared through chemical impregnation (KOH, $ZnCl_2$, H_3PO_4) and one-stage integrated high-temperature pyrolysis. About 30.0 g of cassava peel precursor powder was dissolved in various chemical solutions, including KOH, $ZnCl_2$, and H_3PO_4, at a uniform concentration of 0.5 mol/L, and the solution was placed on a hotplate stirrer with a rotation rate of 300 rpm at 80 °C. The impregnated carbon obtained was dried at 110 °C for 36 h. Chemically impregnated carbon (CIP) is labeled as CIP/K, CIP/Z, and CIP/H according to the use of different impregnation agents KOH, $ZnCl_2$, H_3PO_4. After the carbon and activator agent mixture was completely dry, the powder was compacted using a hydraulic press. About 0.7 g of impregnated powder is placed in a metal mould with a diameter of 2 cm, and the lid of the container is pressed with a hydraulic press with a metric pressure of 8 tons. This process was repeated continuously until 20 solid designs of impregnated carbon precursors were obtained from

each chemical activator agent applied. Subsequently, 20 solid designs of impregnated carbon precursors were fed into a tubular furnace for one-stage integrated high-temperature pyrolysis. Integrated pyrolysis begins with carbonization of N_2 from 30 °C to 600 °C at a gas flow rate of 1.5 mL/min, followed by activation of CO_2 from 601 °C to 850 °C at a flow rate of 0.5 mL/min. The furnace heating rate was controlled at 3 °C/min on N_2 carbonization and 10 °C/min on CO_2 activation. The porous carbon material in the obtained solid design was washed with a solution of hydrochloric acid and deionized water until neutral and dried at 110 °C for 24 h.

2.4. Material characterizations

Dimensional measurements of solid design carbon, including mass, thickness, and radius, were carried out using an electric balance and a calliper, where their values were used to evaluate the density level of solid precursors [38]. Microcrystalline properties were examined by XRD pattern using the Phillip X-Pert-PW3060-10 instrument at λ = 1.5405 Å, recorded at an angle range of 2θ 10–60°. The dimensions of microcrystalline (L_c and L_a) evaluated through Brags' law approach, and the Debye-Scherrer equation was adapted to produce XRD surface area through empirical equations. In addition, through XRD the specific surface area (SSA_{XRD}) can be predicted using empirical equation.

$$d_{002/100} = \frac{n\lambda}{2sin\theta_{002/100}}$$

$$L_c = \frac{0.89\lambda}{\beta cos\theta_{002}}$$

$$L_a = \frac{1.94\lambda}{\beta cos\theta_{100}}$$

$$SSA_{XRD} = \frac{2}{\rho_{XRD}\, L_c}$$

$$\rho_{XRD} = \frac{d_{002\ grphite}}{d_{002\ sample}} \bullet \rho_{graphite}$$

Surface morphology and elemental status of CIPs were observed through scanning electron microscopy and energy dispersive spectroscopy using the JEOL-JSM-6510/LA instrument at 10.00 kV EHT in a spot size of 360. The porosity properties were recorded using the N_2 gas absorption technique and the Quantachrome TouchWin v1.22 instrument. Specific surface area (S_{BET}) was evaluated by using the Brunauer–Emmett–Teller (BET) equation and total volume (V_t) were reviewed by using Dubinin–Radushkevich equation. Meanwhile, micropores surface area (S_{micro}) and micropores volume (V_{micro}) were calculated using a technical t-plot and density functional theory. Mesopores area (S_{meso}), mesopores volume (V_{meso}), and the pore size distribution (PSD) were evaluated using the Barrett–Joyner–Halenda (BJH) equation.

2.5. Electrochemical measurements

The symmetrical supercapacitor was selected as the device to confirm the electrochemical properties of the CIPs electrode and show the original material's real capacitive value. The symmetrical device was prepared with a new design of solid carbon resembling a thin coin separated by an organic membrane of duck egg shell membrane. The supercapacitor cell is designed in 2 × 1 dimensions made of acrylic with a hole in the middle and a diameter of 9 mm. The working mass of the prepared solid electrode was ±9.7 mg in diameter of ±8 mm and a thickness of ±2 mm. The process of preparing the symmetrical supercapacitor design does not use any binder. Furthermore, the electrochemical performance of CIP/s was evaluated through cyclic voltammetry (CV), galvanostatic charge-discharge (GCD), and electrochemical impedance spectroscopy (EIS) tests in a two-electrode configuration system. The CV and GCD techniques were reviewed regarding a potential difference of 0.0 V to 1.0 V at a scan rate of 1 mV s^{-1} with a current density of 1 A g^{-1}. The EIS was measured at amplitude of 10 mV in the frequency range from 0.01 to 100,000 Hz with open-circuit voltage. Specific capacitance (C_{sp}, F g^{-1}), energy density (E_{sp}, Wh kg^{-1}), and power density (P_{sp}, W kg^{-1}) were calculated using the following eq. (1), (2), and (3) [39,40]. From the equation, I and V represented the current (A) and the discharge potential window (V), while t and m were the discharge time (s) and the loading mass of active material (g).

$$C_{sp} = \frac{I \times \Delta t}{m \times \Delta V}$$

$$E_{sp} = \frac{C_{sp} \times \Delta V^2}{7.2}$$

$$P_{sp} = \frac{3600 \times E_{sp}}{\Delta t}$$

3. Result and discussions

The conversion of powdered to solid carbon at an early stage of electrode material synthesis allows precursors to possess high porosity properties without reducing their real conductivity. Due to the chemical impregnation, density evaluation is crucial for examining the evaporation process of volatiles, lignocellulosic chemicals, and the degradation of carbon precursors during the pyrolysis process [41,42]. Fig. 1 illustrates the change in density of solid carbon samples during the high-temperature pyrolysis process. Before pyrolysis, the four samples confirmed almost the same density values of about 0.933 g cm^{-3} at a deviation of ±0.008. The sample without impregnation (Prec-) showed the lowest density change of about 2.30 %. Chemical impregnation significantly confirmed the drastic density changes as shown in CIP/H, CIP/Z, and CIP/K. The impregnation of H_3PO_4 reduces the density of solid carbon to 0.7210 g cm^{-3}. At high temperature, H_3PO_4 reacts with the precursor carbon through an acid hydrolysis process resulting in more pores with P_4, H_2O, and CO as their by-products [43]. The final density of CIP/H samples of about 0.7210 g cm^{-3}. The impregnation of precursor carbon using $ZnCl_2$ resulted in a density reduction of up to 23.70 %. Zinc chloride begins to react with elemental carbon at a pyrolysis temperature of 500 °C to produce ZnOCl and $1/2Cl_2$. Increasing the higher pyrolysis temperature provides energy for ZnOCl to react with C, and it evaporates CO to form different pore structures [44]. The highest density reduction was expressed at CIP/K of 29.01 %. The activating agent KOH reacts with the precursors at temperatures higher than 600 °C, enabling the etching of high carbon chains with their

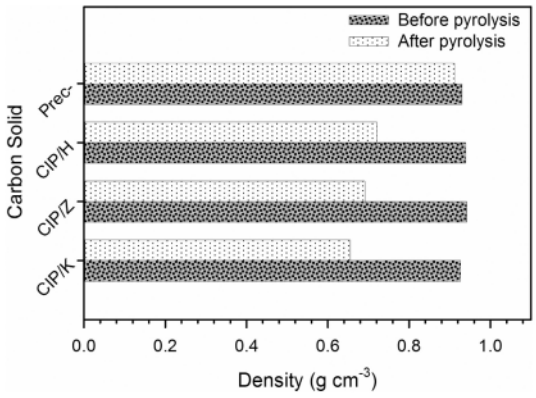

Fig. 1. The density of porous carbon solid CIPs.

reactions repeating up to 6× [45]. Evaporation of volatiles, lignocellulosic components, and removal of final reaction by-products markedly reduced CIP/K densities. It initiated the production of high porosity and showed its great potential for presenting regular pore structures. This analysis was confirmed through the pore size distribution and the morphological structure of the CIPs. Moreover, CO_2, as a physical activating agent, etches the carbon frameworks deeper without any chemical side effects. The combination of this chemical impregnation and physical activation simultaneously results in an excellent porous carbon structure in the electrode material.

After each treatment process, the XRD technique was performed on the samples to ascertain porous carbon's phase and microcrystalline dimensions. The XRD pattern of the CIPs impregnated by different activating agents followed by high-temperature pyrolysis is shown in Fig. 2. The wide peak at angle 2θ in the range 24–25° for the 002 diffraction plane confirmed the weak graphitization properties and coexistence of high amorphous carbon [46]. The 2θ peaks shifted in the 002 diffraction planes 23°, 24°, and 25°, indicating that several inorganic and organic compounds coexist in the solid carbon Prec-, CIP/Z, CIP/K, and CIP/H evaporated simultaneously according to their activating agents. In addition, the organic and inorganic compounds evaporated as a result of chemical impregnation, allowing the formation of carbon enrich-microporous and mesoporous in the sample [47]. This behavior contributes greatly to providing abundant active channels on the electrodes to have a high electrical bilayer. Furthermore, a second broad peak centered at 2θ = 43°–44° correlated with a 100 diffraction plane, confirming that the selected neutralization process significantly removed the organic-inorganic impurities in the carbon derived from the biomass and their activating agents. The solid carbon samples obtained have high amorphous properties that initiate a rich variety of pores. These characteristics greatly improve electrode performance absorbed, CO_2 capture, and energy storage device applications. Microcrystalline dimensions such as d_{002}, d_{100}, L_c, and L_a were reviewed using the Lorentzian equation approach based on the XRD pattern, as summarized in Table 1. The interlayer spacing d_{002} and d_{100} showed values >0.33354 nm graphite revealing that the obtained CIPs samples had properties of high carbon amorphous [48]. Furthermore, the microcrystalline dimensions shown in Table 1 are very low on the order of angstroms revealing that the samples differ significantly beyond the crystalline structure, which can be defined as a turbostratic fully disordered carbon structure [49]. On the other hand, the L_c value can be used to predict the sample surface area, as published in previous studies. According to XRD data, the carbon surface area can be predicted through empirical equations with L_c and d_{002} as their variables. Based on these empirical equations [50,51], chemically impregnated carbon is predicted to have a surface area of >900 $m^2\ g^{-1}$. This analysis is deepened through the analysis of N_2 gas absorption and evaluation of the specific surface area through the BET equation.

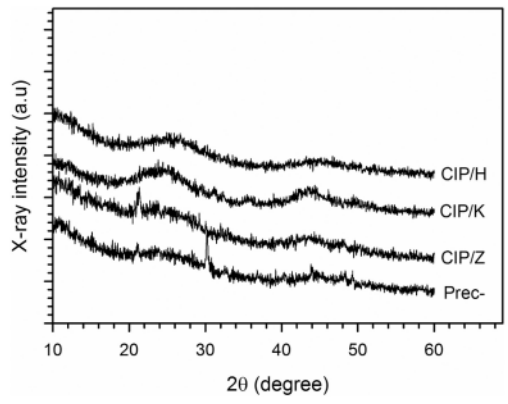

Fig. 2. XRD patterns of porous carbon CIPs.

Table 1
Interlayer spacing of d002 and d100, and microcrystalline dimension of Lc and La.

Porous carbon	$2\theta_{002}$ (°)	$2\theta_{100}$ (°)	d_{002} (Å)	d_{100} (Å)	L_c (Å)	L_a (Å)
Prec-	25.893	44.459	3.43	2.03	10.45	24.83
CIP/Z	24.913	44.762	3.51	2.02	7.53	31.26
CIP/K	22.820	44.765	3.44	2.02	7.80	23.08
CIP/H	24.475	45.928	3.49	1.97	9.72	25.56

The surface morphology of Prec-, CIP/Z, CIP/K and CIP/H carbons were recorded by scanning electron microscopy analysis at various magnifications, as illustrated in Fig. 3. Different chemical impregnation treatments on cassava peel precursors resulted in carbon products with pores that were significantly altered from material lumps and aggregate particles to micro- to nanoscale interconnected pores frameworks. Activating agents that etch carbon chains on lignocellulose components can present a pore framework in CIPs. In addition, high-temperature pyrolysis in the N_2 and CO_2 gaseous environment plays a major role in evaporating their impurities and initiating strong carbon walls, thereby enabling the formation of a hierarchical pore structure [52,53]. The Prec- samples that were non-chemically impregnated showed the morphology of carbon blocks and lumps of particles with a size range of 240-670 μm, as shown in Fig. 3a. The surface is relatively smooth, with very infrequent pore formation confirming poor potential. In contrast to the Prec- sample, the impregnation of H_3PO_4 at CIP/H allows the etching of carbon chains on the sample surface to convert the existing particle aggregates and lumps of material into large dispersed pores. The morphology of CIP/H, as shown in Fig. 3b, illustrates a macroscopic scale pore structure due to the presence of neutralized and evaporated P_4 and CO_2. The pore structure found is in the range of 156-342 nm. The irregular pores indicate that the morphology of the micrographs may be derived from volatile organics and swell expansion, as previously reported [54,55]. Furthermore, the SEM micrograph in Fig. 3c shows a small number of macropores on the inner wall of the hole from CIP/Z, forming an ion buffer reservoir. This property can benefit the insertion/-de-insertion ion during charge-discharge process [56]. In the selected magnification area in Fig. 3d, CIP/Z demonstrated their potential as high porosity carbons in the presence of small irregular pores resembling sponges. This is a consequence of the presence of ZnOCl, which can determine the pore structure of carbonaceous materials. This micrograph significantly triggers high micropores, which are then analyzed more deeply through N_2 gas absorption. The displayed morphological structure allows the sample to have abundant active sites for ions to diffuse on the electrode surface and increases the energy density of the energy storage device. This analysis was further reviewed to confirm the electrochemical properties. Compared to the Prec-, CIP/H, and CIP/Z biocarbon, CIP/K has a rougher surface and flat small aggregate (Fig. 3e). In the low-magnification SEM image, the KOH-impregnated cassava peel biocarbon broke into smaller pieces and showed more folds and pores, resulting from etching their vaporized by-products mainly K_2CO_3 and K_2O. At higher magnifications (Fig. 3f), CIP/K confirmed their surface to be rich in mesoporosity in the diameter size range of 21-49 nm and 57-189 nm. The results were confirmed to be similar through analysis of the surface area and pores size distribution, as summarized in Table 2.

Figs. 4a-d showed the EDS spectra of Prec-, CIP/Z, CIP/K and CIP/H illustrating that their elemental compositional status is dominated by carbon content. According to Table 2, the elemental status of carbon has the highest ratio, around 86–91 %. The Prec- samples possessed the lowest carbon content among the four samples (86 %), with large organic components of calcium and phosphorus at 7 % and 1 %. Chemical impregnation through H_3PO_4, KOH, and $ZnCl_2$ increased the

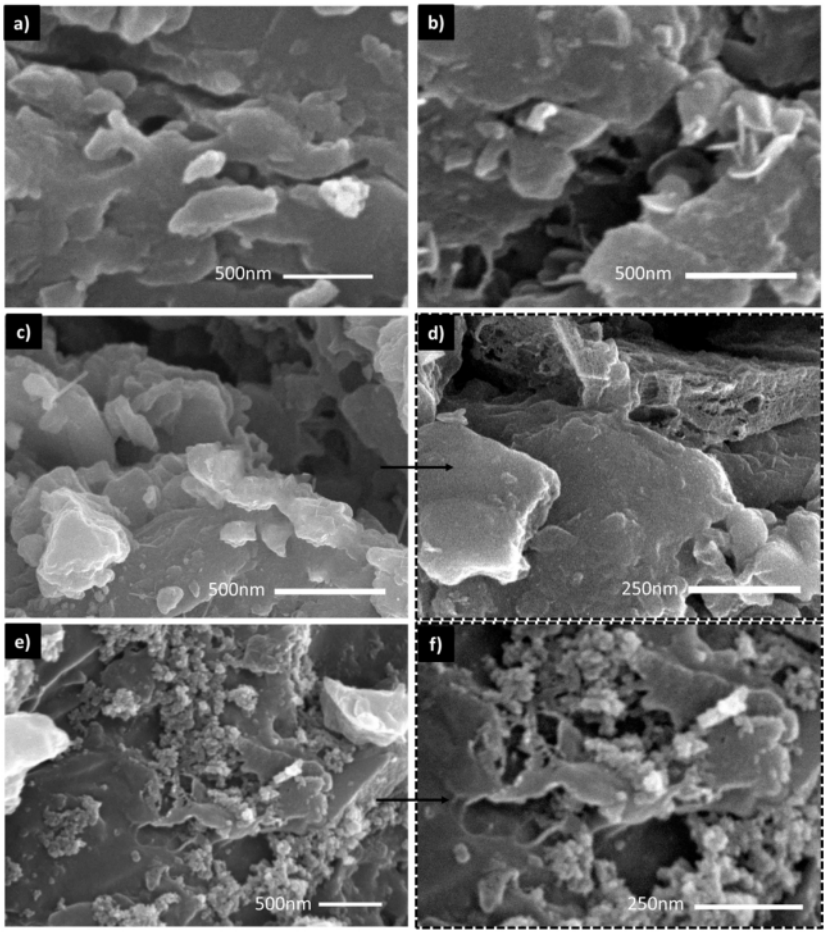

Fig. 3. Micrograph SEM of a) Prec-, b) CIP/H, c) CIP/Z, d) zoom in of c) image SEM, e) CIP/K, and f) zoom in of e) image SEM.

Table 2
Status element and porosity properties Prec-, ZIP/Z, ZIP/K, and ZIP/H.

	Prec-	CIP/Z	CIP/K	CIP/H
Elements				
Carbon (C%)	86.604	94.606	90.747	90.772
Oxygen (O%)	4.748	2.672	4.863	5.143
Phosphor (P%)	7.426	0.000	0.000	0.000
Calcium (Ca%)	1.220	1.557	3.869	3.749
Magnesium (Mg%)	0.000	0.240	0.000	0.334
Zinc (Zn%)	0.000	0.922	0.000	0.000
Potassium (K%)	0.000	0.000	0.519	0.000
Porosity properties				
S_{BET} ($m^2\ g^{-1}$)	280.9	634.7	709.1	333.1
S_{micro} ($m^2\ g^{-1}$)	226.7	595.4	446.4	229.4
S_{meso} ($m^2\ g^{-1}$)	54.2	39.1	262.7	103.7
V_{tot} ($cm^{-3}\ g^{-1}$)	0.163	0.342	0.487	0.213
D_{ave} (nm)	1.166	1.079	1.376	1.282

high carbon content of 90.772 %, 90.747 %, and 94.606 %, respectively. In addition, their dehydrating agent properties significantly reduce the organic precursor component, characterized by the loss of phosphorus elements in CIP/Z, CIP/K, and CIP/H. The by-products of chemical impregnation, such as modest Zn, K, and Ca levels, were still present. However, the neutralization process through HCl and distilled water has been carried out on solid carbon. Elemental oxygen was also confirmed to be quite high in each sample, indicating that the organic components were formed in the state of oxide compounds. The high oxygen content can present the wettability property of the porous carbon, and it initiates self-doping heteroatom to give rise to a pseudo-capacitance effect in supercapacitor devices [15,57]. This analysis was further confirmed through the galvanostatic charge-discharge (GCD) technique.

The surface parameters and pore characteristics of Prec-, CIP/Z, CIP/K, and CIP/H were reviewed using the liquid N_2 adsorption-desorption isotherms at 77 K, as illustrated in Fig. 5a and b. The adsorption-desorption isotherms Prec-, CIP/Z, CIP/K, and CIP/H showed mixed type I and IV characteristics, confirming the micropores-mesopores properties [58,59]. These results significantly confirmed that the micropores of the activated carbon modified carbon increased with the impregnation treatment of $ZnCl_2$, KOH, and H_3PO_4. The isotherms, which increase sharply at a relatively low pressure 'P/P_0' in the 0.01–0.2, indicate that adsorption occurs in the pores of the multimolecular layer [60]. Furthermore, the semi-logarithmic isotherms at relatively higher pressures exhibits the H4 type hysteresis loop characteristics associated with thermochemical activation conditions that allow for multilayer adsorption and complete pore filling during capillary condensation [22,61]. The combination of these two isotherms obtains real information from the presence of various rich micro-

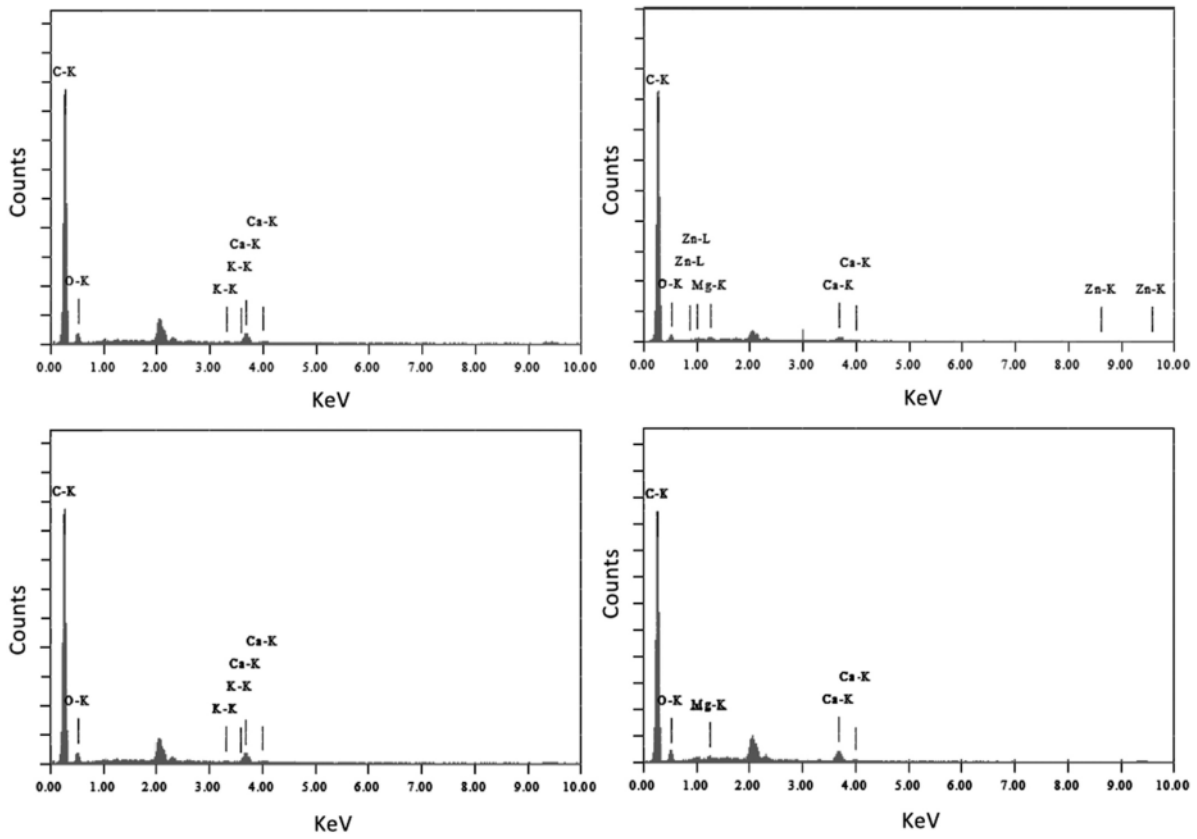

Fig. 4. EDS spectra of a) Prec-, b) CIP/Z, c) CIP/K, and CIP/H.

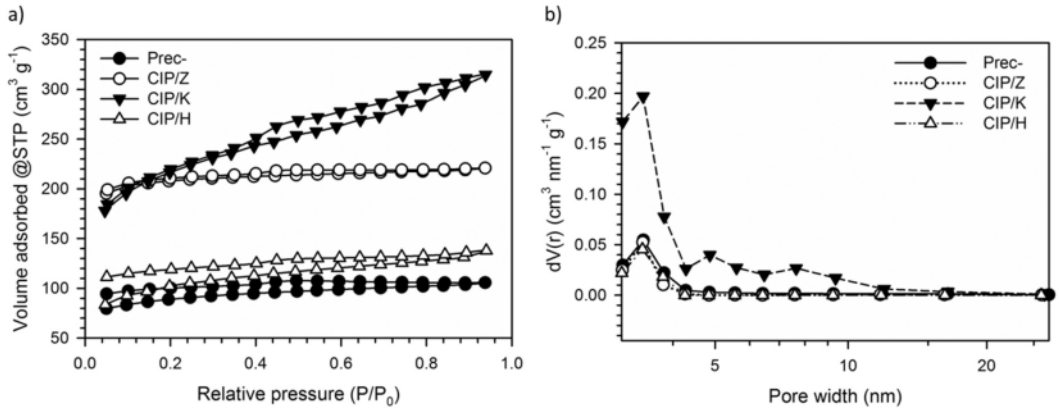

Fig. 5. a) N_2 adsorption isotherms of porous carbon CIPs, and b) BJH desorption pore size distributions of porous carbon CIPs.

mesopores of the four samples. Prec- sample displays the lowest isotherms with an open hysteresis loop, indicating that the sample has poor mesopores. Meanwhile, mesopores are not completely formed, where their pore surface is relatively narrow and the pore base is relatively wide [62]. This confirms that the chemically impregnated samples tend to have unfavorable pore conditions. CIP/H also showed similar isotherms characteristics, but their adsorption was greater than Prec-. The impregnation of H_3PO_4 on solid carbon samples was insufficient to obtain a high micro-mesopores structure, as shown in Fig. 5a. Meanwhile, the impregnation of $ZnCl_2$ displayed a high isotherm with a rich micropores structure, as shown in Table 2. A closed narrow hysteresis loop initiating mesopores was completely formed, although in relatively low amounts. The CIP/K isotherms are associated with an H4-type hysteresis loop with steep graphs at lower relative pressures confirming a high surface area with a combination of high micropores and mesopores [63]. Micropores reduction allows the KOH activating agent

50 tch the carbon to produce more mesopores. The texture properties, including BET surface area, micropores surface area, mesopores surface area, total volume, and average pore diameter, are summarized in Table 2. Specific surface area significantly increased after chemical impregnation treatment 38 at high-temperature pyrolysis. The precursor sample showed a low surface area of 280.9 $m^2 g^{-1}$ with a total volume of 0.164 $cm^3 g^{-1}$. Meanwhile, impregnation of H_3PO_4, $ZnCl_2$, and KOH dramatically increased the surface area from 333.1 to 709.1 $m^2 g^{-1}$ with a maximum volume of 0.488 $cm^3 g^{-1}$. The micropores evaluated by t-Plot also experienced the same result with a variable increase with the volume ranging from 0.129 to 0.483 $cm^3 g^{-1}$. Therefore, CIP/Z has a high micro-surface area of 93.83 %, followed by CIP/K, CIP/H, and Prec-. Combined with the SEM image results, the increase in micropores in the carbon enhanced through chemical impregnation promotes a pore formation reaction between the hydrochar and the activator. The many active channels made possible by the activated carbon's extreme microporosity assist the creation of a highly rigid electrical layer on the electrode [64]. This property markedly increases the symmetric supercapacitor device's specific capacitance and energy density. Mesoporosity confirmation of Prec-, CIP/Z, CIP/K, and CIP/H was examined in detail through the pore size distribution of the BJH technique, as shown in Fig. 5b. These results have similar trends to the previous literature. The activated carbon from KOH impregnation showed higher mesoporosity content and higher surface area due to intercalation of activated K molecules with carbon lattice and matrix than activated carbon $ZnCl_2$ and H_3PO_4.

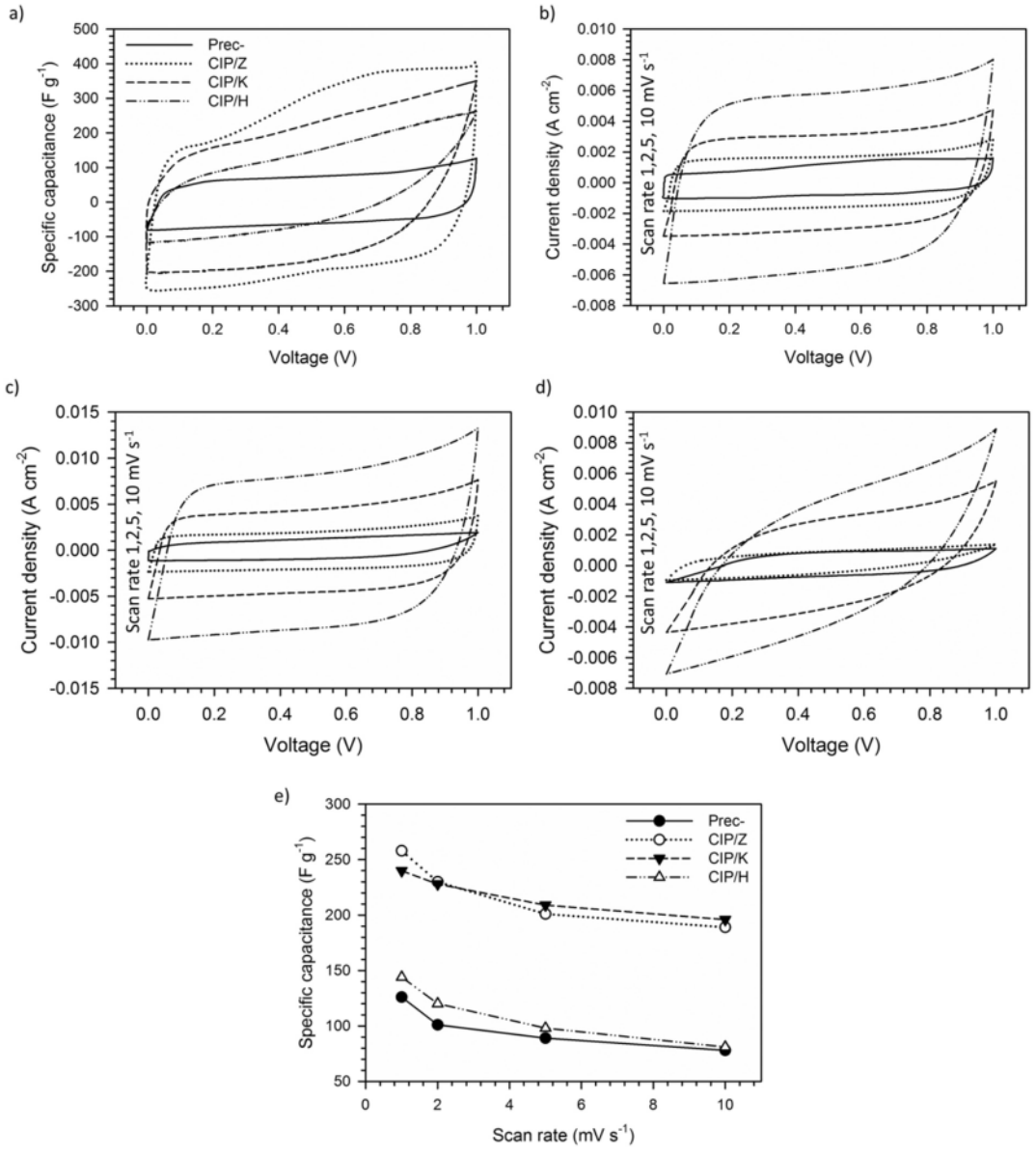

Fig. 6. a) CV curve of porous carbon CIPs at 1 mV s^{-1}, CV curve at different scan rate of b) CIP/K, c) CIP/Z, d) CIP/H, e) specific vs. scan rate of porous carbon CIPs.

The electrochemical performance of Prec-, CIP/Z, CIP/K, and CIP/H was investigated completely through cyclic voltammetry, galvanostatic charge-discharge, and electrochemical impedance spectroscopy techniques in a two-electrode configuration system with 1 M H_2SO_4 aqueous electrolyte. The CV method was used to study the electrochemical behavior of CIPs electrodes at potential intervals from 0.0 to 1.0 V in various scanning levels of 1–20 mV s^{-1}. At a scan rate of 1 mV s^{-1}, the CIPs electrode displayed a CV curve with a swift specific capacitance response at a very low voltage of 0.09 V, reflecting the fast ionic diffusion in the electrolyte towards the electrode surface (Fig. 6a) [65]. The ions fill the micropores forming a rigid charge layer at the electrode/electrolyte interface. The capacitance response subsides at a potential >0.2 V initiating ion insertion in larger pores up to a maximum potential of 1.0 V. Fig. 6a, and the CIPS CV curve shows a rectangular shape with slight distortion, confirming the normal double layer electrochemical properties of the biomass-based carbon material. Compared to other samples, CIP/Z presents a wider rectangular shape revealing more double-layer capacitance and is followed by a hump at 0.2–0.8 V potential, confirming the effect of extra pseudo capacitance originating from self-doping heteroatoms [15,66]. The apparent capacitance is indicated by the presence of oxygen in the carbon skeleton. In addition, CIP/K displays a leaf-like CV curve with a sudden capacitance response at a potential of 0.2–0.9 V, reflecting the ion insertion/de-insertion process in a balanced micro-mesopores initiating the best double layer electrochemistry [67]. A similar characteristic curve is also shown in CIP/H, but the capacitance response in the discharge process characterizes poor pore properties. Prec- samples have the lowest specific capacitance response curve indicating their low material properties to enhance the electrochemical properties of the supercapacitor electrodes. Therefore, this analysis shows that the CIP/Z sample has the highest specific capacitance, followed by CIP/K, CIP/H, and Prec-. The surface structure that presents hierarchical pores followed by heteroatom doping is a strong reason for the CIP/Z electrodes to show high electrochemical performance. The CV profiles of the CIPs were reviewed at a larger scan rate, as shown in Fig. 6b-d. The CV profiles are confirmed to retain a rectangular shape even though their distortion increases with each scan level. This is due to the resistance of the electrode material, and an in-depth analysis was reviewed through the Nyquist plot. Interestingly, CIP/Z is consistent in rectangles even at a scan speed of 20 mV s^{-1}, implying more excellent energy storage capabilities than CIP/K, CIP/H and Prec-. The specific capacitance responses at different scan rates of the Prec-, CIP/Z, CIP/K, and CIP/H electrodes are shown in Fig. 6e. The magnified scan rate significantly reduces their capacitive properties due to the electrode resistance and ion diffusion. However, the CIP/Z electrode can maintain a high capacitance of 191 F g^{-1} at a scan rate of 20 mV s^{-1} at a 76 % rate capability. These outcomes are comparable to the carbon-based electrodes' responses to banana leaf biomass and sakura flowers [30,41].

The specific capacitance energy and power of the CIPs electrode were revealed in detail through the analysis of the GCD profile, as shown in Figs. 7a-d. Fig. 6a shows an almost ideal isosceles triangular shape with a very small iR revealing that the CIPs electrode has a rigid electrical bilayer property with low electrode resistance in an aqueous electrolyte at a current density of 1 A g^{-1} [68]. Furthermore, their confirmed

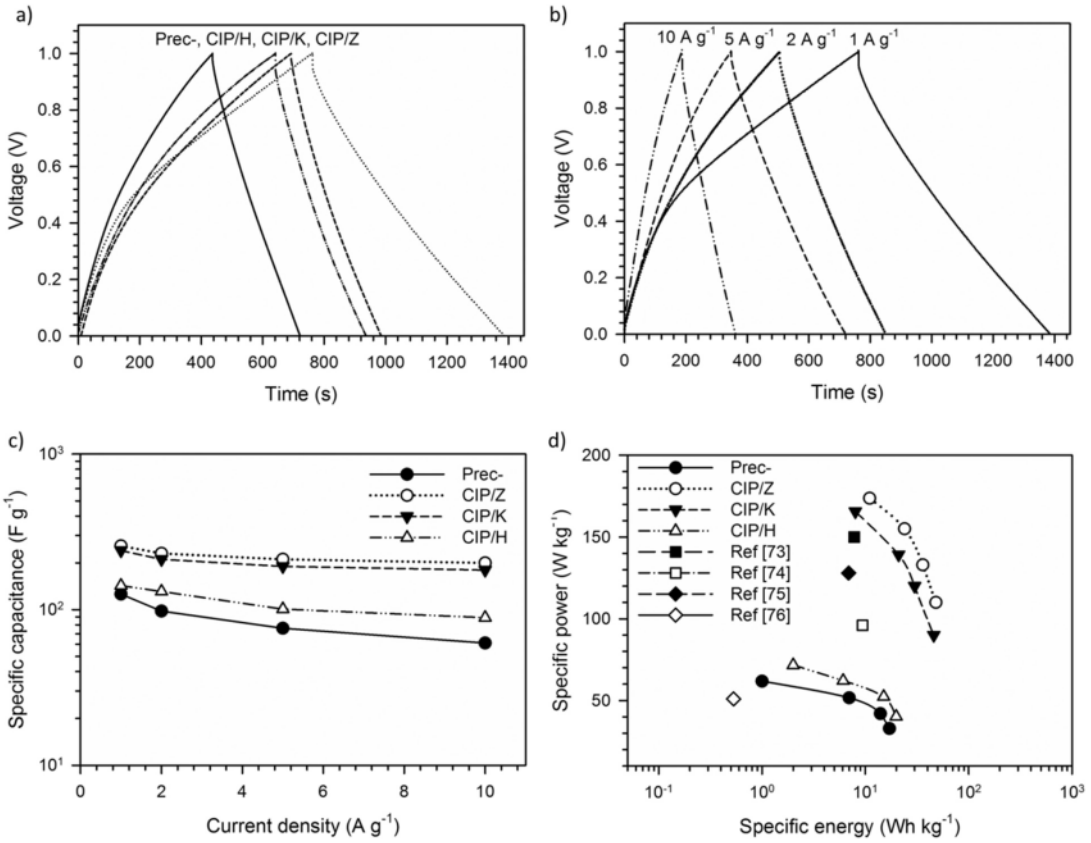

Fig. 7. a) GCD curve of porous carbon CIPs at 1 A g^{-1}, b) GCD curve of CIP/Z at different current density, c) specific capacitance vs. current density, and d) Ragone plot of porous carbon CIPs.

coulombic efficiencies in the range of 75–89 % showed that the CIPs electrode has extra pseudocapacitance properties as part of the contribution of high wettability and heteroatom doping [69]. This property is indicated by the high oxygen heteroatoms, as summarized in Table 2, which is a major contributor to the self-doping of the electrode material [70]. The length of charge-discharge time of the GCD profiles reflects their capacitive nature. CIP/Z displays the longest charging and discharging process, confirming the highest capacitive properties of 257 F g^{-1}. The porosity properties of the CIP/Z electrode, which has a high micropore surface area, allow the electrode to provide abundant active sites. Therefore, the ionic charges form a large electrical double layer. The surface structure exhibiting a connected hierarchical pore resembling a sponge initiates fine ion insertion/de-insertion to enhance electrochemical performance. In addition, the wettability of the oxygen allows CIP/Z to have self-doping heteroatoms adding to its extra-pseudo-capacitance properties. These characteristics significantly present a high specific capacitance at the CIP/Z electrode. CIP/K has the next highest specific capacitance, at 240 F g^{-1}. The highest surface area contribution initiating the CIP/Z electrode showed the highest capacitive properties after CIP/K. CIP/H and Prec- occupy low capacitive properties around 143 and 126 F g^{-1}, respectively. Low porosity and poor pore structure permit restricted ion diffusion space and reduced charge transfer paths. However, the specific capacitance can be maintained at 56.01 %, 62.23 %, 77.82 and 92.43 % when the current density is increased from 1 to 10 A g^{-1} for Prec-, CIP/H, CIP/K, and CIP/Z. These results indicate that the CIPs electrode has good EDLC device rate capability, as shown in Fig. 7c. The electrode maintains a coulombic efficiency of up to 91.10 % at a current density of 10 A g^{-1}, implying that the device has excellent stability [71,72]. A Ragone plot of EDLC CIPs based on cassava peel biomass and comparison with other carbonaceous materials is shown in Fig. 7d. The best EDLC CIPs were found on the CIP/Z electrode, which displayed the highest specific energy of 35.69 Wh kg^{-1} at a specific power of 167.68 W kg^{-1}. Meanwhile, the electrodes CIP/K, CIP/H, and Prec had specific energies of 33.33, 19.87, and 17.13 Wh kg^{-1} at specific powers of 152.73, 71.70, and 61.82 W kg^{-1}, respectively. These results are comparable to other carbon-based electrodes, such as rice straw [73], pamelo peel [74], bacterial cellulose [75], and native European deciduous trees [76]. The comparisons of the capacitive behavior parameters of the CIP/Z electrode with several biomass-based porous carbon sources in detail are shown in Table 3.

The electrochemical performance of the symmetrical supercapacitor device based on carbonaceous CIPs on aqueous electrolytes was confirmed in more detail by EIS analysis, as summarized in Fig. 8a-c. Fig. 8a shows a Nyquist plot of CIPs electrodes on the Corrtest Studio v6.0 software in an open circuit potential at the frequency range from 100,000 Hz to 0.01 Hz. The Nyquist curve displays a semicircle in the high-frequency region, followed by a straight line in the low-frequency to reflect the charge transfer resistance of the electrolyte ions and their diffusion in the electrode pores. From the Nyquist curve, the CIPs symmetrical device displays a relatively low electrolyte solution resistance (R_s) in the range of 0.13–0.96 Ω. This revealed that the self-doping heteroatoms on the electrode surface increased the wettability of the sample to the electrolyte. Furthermore, differences in chemical activating agents significantly affect the electrochemical properties of the electrodes. The performance of the CIP/Z electrode showed the lowest electrolytic ion charge diffusion resistance (R_{ct}) of 0.63 Ω due to the hierarchical pore structure with a balanced proportion of micro-mesopores and self-doping heteroatoms contributing highly to charge transfer and barrier-free diffusion of electrolyte ions [68,77]. The CIP/K electrode displays the lowest Rs of 0.13 Ω with an R_{ct} of around 2.76 Ω, and the pore-rich sample surfaces can enhance electrochemical properties. Furthermore, CIP/H and Prec- electrodes display relatively large cell resistance confirming their poor electrochemical performance. Moreover, the equivalent series resistance of Prec-, ZIP/Z, ZIP/K, and ZIP/H were 29.3, 8.9, 9.2, and 15.3 Ω, respectively. Fig. 8b shows the CIPs bode plot of the apparent capacitance (C′) as a frequency function evaluating how many electrolyte ions reach the porous carbon interface in a given frequency region. At low frequencies, the CIP/K electrodes display high capacitance, followed by CIP/Z, CIP/H, and Prec-, revealing that their entire surface is accessible to electrolyte ions. It exhibits a slower decrease in capacitance at a higher frequency, indicating an effective ion migration phenomenon. This proves the importance of the electrode having spilt microporosity as the small ion pathway required to achieve higher performance. Fig. 8c presents a plot of the imaginary capacitance (C″) as a frequency function, representing the relaxation time constant. This parameter confirms the minimum time required to efficiently discharge the energy device voltage. The relaxation time constant was evaluated using the equation $\tau = 1/2\pi f_p$, where f_p is the peak frequency of each CIP electrode [78]. The CIP/Z electrode showed the shortest relaxation time of 18.51 ms, followed by CIP/K, CIP/H and Prec- 24.63, 62.50, and 79.30 ms, respectively. Therefore, the symmetrical electrodes of CIPs have ultra-fast and excellent ion adsorption/desorption rates. The electrochemical studies through joint CV, GCD and EIS analysis accompanied by their detailed plots and profiles show that the carbon structure with hierarchical pore morphology, rich in micropores and self-doping heteroatoms, facilitates the creation of abundant electrical layers, smoothly initiating ion migration.

4. Conclusion

A series of porous carbon-based electrode materials with 3D hierarchical pore structure and heteroatom doping have been successfully optimized from cassava peel biomass. The porous carbon was prepared using the chemical immersion route, N_2 carbonization, and CO_2 physical activation. The pore structure and surface morphology were controlled through activating agents including $ZnCl_2$, KOH, and H_3PO_4. In addition, the working electrode is designed to resemble a solid coin without a binder. Surface morphological studies of the $ZnCl_2$ impregnated carbon confirmed macrospore pores with diameters of 50–89 nm, and micro-scale pores in their walls were 3D hierarchically connected. Furthermore, the predominant micropores and the highest carbon level enhance the superior material properties of the chemically impregnated carbon $ZnCl_2$. KOH impregnation displays a diverse pore structure with a dominant combination of macro-mesopores, while the H_3PO_4 activator agent tends to display an unfavorable morphological structure. A thorough electrochemical analysis showed that physical parameters were very influential in improving the performance of the electrode,

Table 3
Comparison of the capacitive performance of CIP/Z electrode with other biomass derived porous carbon materials.

Sources	Morphology	Dopant	Electrode system	Electrolyte	C_{sp} (F g^{-1})	E_{sp} (Wh kg^{-1})	P_{sp} (W kg^{-1})	Ref
Watermelon peel	Hierarchical	N-doped	2-Electrode	1 M H_2SO_4	226	25.4	180	[29]
Sakura petals	3D honeycomb	N-O-doped	2-Electrode	6 M KOH	265	–	–	[30]
Ginger	Hierarchical	N-S-doped	2-Electrode	1 M H_2SO_4	348	48.3	400	[31]
Rice straw	–	–	2-Electrode	1 M H_2SO_4	156	7.8	150.2	[73]
European deciduous tree	Honeycomb-like	–	2-Electrode	1 M H_2SO_4	24	0.53	51	[76]
Eucalyptus-bark	Hierarchical	–	2-Electrode	1 M H_2SO_4	155	32.8	57 k	[77]
Cassava peel	Hierarchical	O-doped	2-Electrode	1 M H_2SO_4	257	35.69	167.68	This study

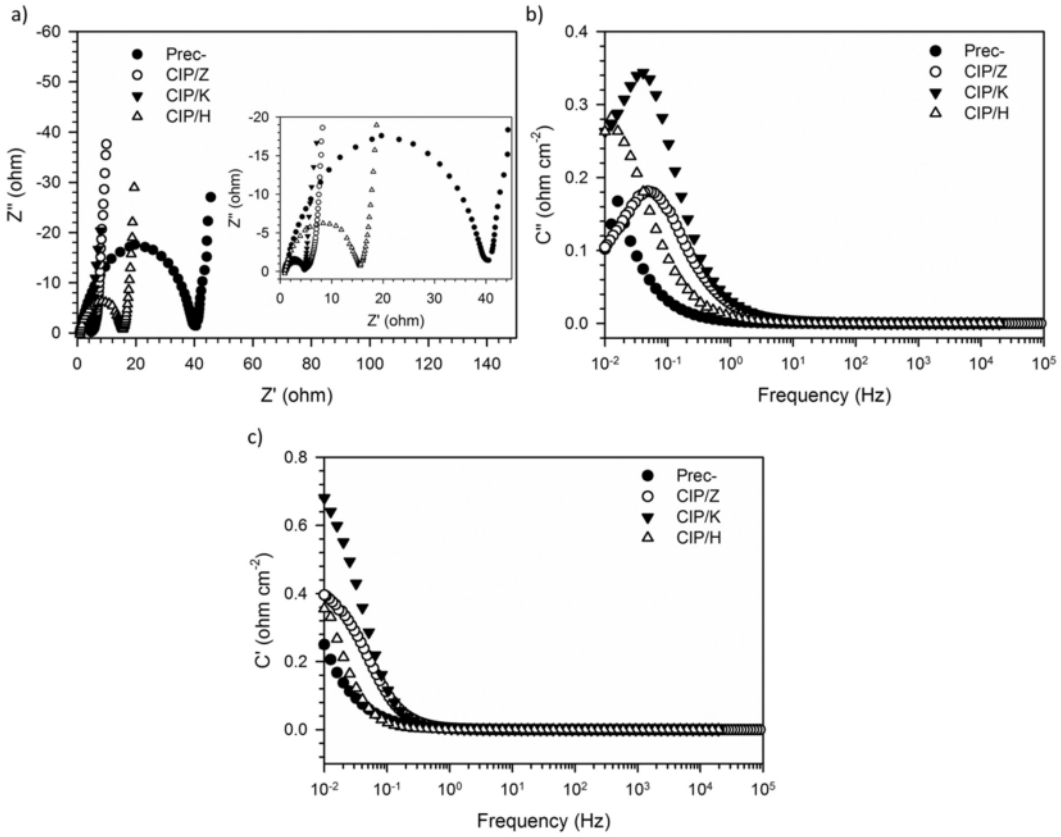

Fig. 8. a) Nyquist plot, b) Bode plot of real capacitance vs. frequency, and c) Bode plot of imaginer capacitance vs. frequency of porous carbon CIPs.

including 3D hierarchical pores dominated by micropores (up to 94 %), high carbon content (86,604-94,606 %), and enriched self-doping of oxygen functional groups (2672–5.143 %). These features are needed to extract the best performance from cassava peel-based activated carbon as an electrode material with high capacitive properties, low charge transfer resistance, fast ion adsorption/desorption, high rate capability, and enhanced energy density. The optimized electrode from CIP/Z has the best electrochemical properties with a specific capacitance of 257 F g^{-1} in 1 M H_2SO_4. It possessed low electrolyte solution resistance (R_s) in the range of 0.13–0.96 Ω and low electrolytic ion charge diffusion resistance (R_{ct}) of 0.63 Ω. In conclusion, it is hoped that this article will provide scientific information regarding the optimization of electrode materials from cassava peel-based activated carbon for supercapacitor applications.

CRediT authorship contribution statement

Eva Wahyuni Harahap: Resources, Data curation, Writing - Original draft preparation, **Erman Taer:** Conceptualization, Methodology, **Ari Sulistyo Rini:** Data curation, **Rika Taslim:** Visualization, Validation, **Apriwandi Apriwandi:** Formal analysis, Writing - Original draft preparation, Data curation, Writing - Reviewing & Editing.

Declaration of competing interest

The authors declare that they have no known competing financial interests or personal relationships that could have appeared to influence the work reported in this paper.

Data availability

Data will be made available on request.

Acknowledgements

The research was funded by *Direktorat Jenderal Pendidikan Tinggi, Riset dan Teknologi*, Republic of Indonesia in master thesis research-postgraduate program scheme, contract No.: 1657/UN19.5.1.3/PT.01.03/2022.

References

[1] L. Zhang, X.S. Zhao, Carbon-based materials as supercapacitor electrodes, Chem. Soc. Rev. 38 (2009) 2520–2531, https://doi.org/10.1039/b813846j.
[2] P. Pramanik, H. Patel, S. Charola, S. Neogi, S. Maiti, High surface area porous carbon from cotton stalk agro-residue for CO2 adsorption and study of techno-economic viability of commercial production, J. CO2 Util. 45 (2021), 101450, https://doi.org/10.1016/j.jcou.2021.101450.
[3] N. Abuelnoor, A. AlHajaj, M. Khaleel, L.F. Vega, M.R.M. Abu-Zahra, Activated carbons from biomass-based sources for CO2 capture applications, Chemosphere 282 (2021), 131111, https://doi.org/10.1016/j.chemosphere.2021.131111.
[4] J. Chen, L. Dai, Carbon nanomaterials for high-performance supercapacitors, Mater. Today 16 (2013) 272–280, https://doi.org/10.1016/j.mattod.2013.07.002.
[5] Poonam, K. Sharma, A. Arora, S.K. Tripathi, Review of supercapacitors: materials and devices, J. Energy Storage 21 (2019) 801–825, https://doi.org/10.1016/j.est.2019.01.010.
[6] W. Du, L. Miao, Z. Song, X. Zheng, Y. Lv, D. Zhu, L. Gan, M. Liu, Kinetics-driven design of 3D VN/MXene composite structure for superior zinc storage and charge transfer, J. Power Sources 536 (2022), 231512.
[7] P. Simon, Y. Gogotsi, Charge storage mechanism in nanoporous carbons and its consequence for electrical double layer capacitors, Philos. Trans. R. Soc. A Math. Phys. Eng. Sci. 368 (2010) 3457–3467, https://doi.org/10.1098/rsta.2010.0109.

[8] Y. Qin, L. Miao, M. Mansuer, C. Hu, Y. Lv, L. Gan, M. Liu, Spatial confinement strategy for micelle-size-mediated modulation of mesopores in hierarchical porous carbon nanosheets with an efficient capacitive response, ACS Appl. Mater. Interfaces 14 (2022) 33328–33339.

[9] H. Yang, S. Ye, J. Zhou, T. Liang, Biomass-derived porous carbon materials for supercapacitor, Front. Chem. 7 (2019) 1–17, https://doi.org/10.3389/fchem.2019.00274.

[10] E.E. Miller, Y. Hua, F.H. Tezel, Materials for energy storage: review of electrode materials and methods of increasing capacitance for supercapacitors, J. Energy Storage 20 (2018) 30–40, https://doi.org/10.1016/j.est.2018.08.009.

[11] A. Yu, V. Chabot, J. Zhang, Electrochemical Supercapacitors for Energy Storage and Delivery, 2013.

[12] M. Yassine, D. Fabris, Performance of commercially available supercapacitors, Energies 10 (2017) 340, https://doi.org/10.3390/en10091340.

[13] H. Wang, C. Wang, Y. Xiong, C. Jin, Q. Sun, Simple synthesis of N-doped interconnected porous carbon from chinese tofu for high-performance supercapacitor and lithium-ion battery applications, J. Electrochem. Soc. 164 (2017) A3832–A3839, https://doi.org/10.1149/2.1401714jes.

[14] Z. Song, L. Miao, L. Ma, D. Zhu, L. Gan, M. Liu, A robust strategy of solvent choice to synthesize optimal nanostructured carbon for efficient energy storage, Carbon 180 (2021) 135–145, https://doi.org/10.1016/j.carbon.2021.04.078.

[15] E. Taer, R. Taslim, A. Apriwandi, Ultrahigh capacitive supercapacitor derived from self-oxygen doped biomass-based 3D porous carbon sources, ChemNanoMat. 8 (2022), e202100388, https://doi.org/10.1002/cnma.202100388.

[16] Q. Abbas, R. Raza, I. Shabbir, A.G. Olabi, Heteroatom doped high porosity carbon nanomaterials as electrodes for energy storage in electrochemical capacitors: a review, J. Sci. Adv. Mater. Devices 4 (2019) 341–352, https://doi.org/10.1016/j.jsamd.2019.07.007.

[17] A. Gopalakrishnan, C.Y. Kong, S. Badhulika, Scalable, large-area synthesis of heteroatom-doped few-layer graphene-like microporous carbon nanosheets from biomass for high-capacitance supercapacitors, New J. Chem. 43 (2019) 1189–1194, https://doi.org/10.1039/c8nj05128c.

[18] Z. Song, H. Duan, L. Miao, L. Ruhlmann, Y. Lv, W. Xiong, D. Zhu, L. Li, L. Gan, M. Liu, Carbon hydrangeas with typical ionic liquid matched pores for advanced supercapacitors, Carbon 168 (2020) 499–507, https://doi.org/10.1016/j.carbon.2020.07.004.

[19] Y. Bai, R. Liu, Li, X. Li, Y. Liu, G. Yuan, Graphene/Carbon Nanotube/Bacterial cellulose assisted supporting for polypyrrole towards flexible supercapacitor applications, J. Alloys Compd. 777 (2019) 524–530, https://doi.org/10.1016/j.jallcom.2018.10.376.

[20] Z. Song, D. Zhu, L. Li, T. Chen, H. Duan, Z. Wang, Y. Lv, W. Xiong, M. Liu, L. Gan, Ultrahigh energy density of O, S, O codoped carbon nanosphere based all-solid-state symmetric supercapacitor, J. Mater. Chem. A 7 (2019) 1177–1186, https://doi.org/10.1039/c8ta10158b.

[21] A. Gopalakrishnan, S. Badhulika, Sulfonated porous carbon nanosheets derived from oak nutshell based high-performance supercapacitor for powering electronic devices, Renew. Energy 161 (2020) 173–183, https://doi.org/10.1016/j.renene.2020.06.004.

[22] K. Aruchamy, K. Dharmalingam, C.W. Lee, D. Mondal, N. Sanna Kotrappanavar, Creating ultrahigh surface area functional carbon from biomass for high performance supercapacitor and facile removal of emerging pollutants, Chem. Eng. J. 427 (2022), 131477, https://doi.org/10.1016/j.cej.2021.131477.

[23] C. Ding, T. Liu, X. Yan, Z. Huang, S. Ryu, J. Lan, Y. Yu, W.H. Zhong, X. Yang, AN ultra-microporous carbon material boosting integrated capacitance for cellulose-based supercapacitors, Nano-Micro Lett. 12 (2020) 63, https://doi.org/10.1007/s40820-020-0393-7.

[24] X. Liang, R. Liu, X. Wu, Biomass waste derived functionalized hierarchical porous carbon with high gravimetric and volumetric capacitances for supercapacitors, Microporous Mesoporous Mater. 310 (2021), 110659, https://doi.org/10.1016/j.micromeso.2020.110659.

[25] S. Majid, A.S.G. Ali, W.Q. Cao, R. Reza, Q. Ge, Biomass-derived porous carbons as supercapacitor electrodes-a review, New Carbon Mater. 36 (2021) 546–572, https://doi.org/10.1016/S1872-5805(21)60038-0.

[26] E. Taer, R. Taslim, Brief review: preparation techniques of biomass based activated carbon monolith electrode for supercapacitor applications, in: AIP Conf. Proc, 2018, pp. 020004-1–020004-4, https://doi.org/10.1063/1.5021192.

[27] T. Wang, A.H. Rony, K. Sun, S.J. Smith, G. Eddings, M. Fan, T. Wang, A.H. Rony, K. Sun, W. Gong, X. He, W. Lu, M. Tang, Carbon nanofibers prepared from solar pyrolysis of pinewood as binder-free electrodes for flexible supercapacitors, Cell Rep.Phys. Sci. 1 (2020), 100079, https://doi.org/10.1016/j.xcrp.2020.100079.

[28] Y. Xi, J. Cao, J. Li, P. Zhang, Y. Zhu, W. Han, High-rate supercapacitor based on 3D hierarchical N-doped porous carbon derived from sustainable spongy cornstalk pith, J. Energy Storage 37 (2021), 102470, https://doi.org/10.1016/j.est.2021.102470.

[29] P. Zhang, J. Mu, Z. Guo, S.I. Wong, J. Sunarso, Y. Zhao, W. Xing, J. Zhou, S. Zhuo, Watermelon peel-derived heteroatom-doped hierarchical porous carbon as a high-performance electrode material for supercapacitors, ChemElectroChem. 8 (2021) 1196–1203, https://doi.org/10.1002/celc.202100267.

[30] F. Ma, S. Ding, H. Ren, Y. Liu, Sakura-based activated carbon preparation and its performance in supercapacitor applications, RSC Adv. 9 (2019) 2474–2483, https://doi.org/10.1039/c8ra09685f.

[31] A. Gopalakrishnan, T.D. Raju, S. Badhulika, Green synthesis of nitrogen, sulfur-co-doped worm-like hierarchical porous carbon derived from for outstanding supercapacitor performance, Carbon 168 (2020) 209–219, https://doi.org/10.1016/j.carbon.2020.07.017.

[32] Y. Lin, Z. Chen, C. Yu, W. Zhong, Facile synthesis of high nitrogen-doped content, mesopore-dominated biomass-derived hierarchical porous graphitic carbon for high performance supercapacitors, Electrochim. Acta 334 (2020), 135615, https://doi.org/10.1016/j.electacta.2020.135615.

[33] Z. Daud, H. Awang, A.S.M. Kassim, M.Z.M. Hatta, A.M. Aripin, Comparison of pineapple leaf and cassava peel by chemical properties and morphology characterization, Adv. Mater. Res. 974 (2014) 384–388, https://doi.org/10.4028/www.scientific.net/AMR.974.384.

[34] E. Taer, Apriwandi, B.K.L. Dalimunthe, R. Taslim, A rod-like mesoporous carbon derived from agro-industrial cassava petiole waste for supercapacitor application, J. Chem. Technol. Biotechnol. 96 (2021) 662–671, https://doi.org/10.1002/jctb.6579.

[35] A.E. Ismanto, S. Wang, F.E. Soetaredjo, S. Ismadji, Preparation of capacitor's electrode from cassava peel waste, Bioresour. Technol. 101 (2010) 3534–3540.

[36] J. Ospino, J.P. Parra-Barraza, S. Cervera, E.E. Coral-Escobar, O.A. Vargas-Ceballos, Activated carbon from cassava peel: a promising electrode material for supercapacitors, Rev. Fac. Ing. (2022) 88–95, https://doi.org/10.17533/udea.redin.20200803.

[37] T.F. Amakoromo, O.E. Abumere, J.A. Amusan, V. Anye, A. Bello, Porous carbon from Manihot Esculenta (cassava) peels waste for charge storage applications, Curr. Res. Green Sustain. Chem. 4 (2021), 100098, https://doi.org/10.1016/j.crgsc.2021.100098.

[38] E. Taer, Farma, M. Deraman, R. Omar, M.M. Awitdrus, E. Ishak, I.A.Talib Taer, Binderless composite electrode monolith from carbon nanotube and biomass carbon activated by KOH and CO2 gas for supercapacitor, AIP Conf. Proc. 1415 (2011) 180–184, https://doi.org/10.1063/1.3667251.

[39] Q. Zhang, K. Han, S. Li, M. Li, J. Li, K. Ren, Synthesis of garlic skin-derived 3D hierarchical porous carbon for high-performance supercapacitors, Nanoscale 10 (2018) 2427–2437, https://doi.org/10.1039/c7nr07158b.

[40] S.S. Gunasekaran, A. Gopalakrishnan, R. Subashchandrabose, S. Badhulika, Single step, direct pyrolysis assisted synthesis of nitrogen-doped porous carbon nanosheets derived from bamboo wood for high energy density asymmetric supercapacitor, J. Energy Storage 42 (2021), 103048, https://doi.org/10.1016/j.est.2021.103048.

[41] A. Apriwandi, E. Taer, R. Farma, R.N. Setiadi, E. Amiruddin, A facile approach of micro-mesopores structure binder-free coin/monolith solid design activated carbon for electrode supercapacitor, J. Energy Storage 40 (2021), 102823, https://doi.org/10.1016/j.est.2021.102823.

[42] E. Taer, N. Yanti, W.S. Mustika, A. Apriwandi, R. Taslim, A. Agustino, Porous activated carbon monolith with nanosheet/nanofiber structure derived from the green stem of cassava for supercapacitor application, Int. J. Energy Res. 44 (2020) 9204, https://doi.org/10.1002/er.5639.

[43] A. Elmouwahidi, E. Bailón-García, A.F. Pérez-Cadenas, F.J. Maldonado-Hódar, F. Carrasco-Marín, Activated carbons from KOH and H3PO4-activation of olive residues and its application as supercapacitor electrodes, Electrochim. Acta 229 (2017) 219–228, https://doi.org/10.1016/j.electacta.2017.01.152.

[44] P. Kalyani, A. Anitha, Biomass carbon & its prospects in electrochemical energy systems, Int. J. Hydrog. Energy 38 (2013) 4034–4045, https://doi.org/10.1016/j.ijhydene.2013.01.048.

[45] W. Jiang, J. Pan, X. Liu, A novel rod-like porous carbon with ordered hierarchical pore structure prepared from Al-based metal-organic framework without template as great enhanced performance for supercapacitor, J. Power Sources 409 (2019) 13–23, https://doi.org/10.1016/j.jpowsour.2018.10.086.

[46] S. Saha, D. Potphode, C.S. Sharma, Borassus flabellifer fruit flesh derived hierarchical porous partly graphitic carbon as a sustainable electrode for supercapacitors, Energy Fuel 36 (2022) 638–654.

[47] L.H. Zheng, M.H. Chen, S.X. Liang, Q.F. Lü, Oxygen-rich hierarchical porous carbon derived from biomass waste-kapok flower for supercapacitor electrode, Diam. Relat. Mater. 113 (2021), 108267, https://doi.org/10.1016/j.diamond.2021.108267.

[48] J. Serafin, M. Baca, J. Biegun, E. Mijowska, R.J. Kaleńczuk, J. Sreńscek-Nazzal, B. Michalkiewicz, Direct conversion of biomass to nanoporous activated biocarbons for high CO2 adsorption and supercapacitor applications, Appl. Surf. Sci. 497 (2019), 143722, https://doi.org/10.1016/j.apsusc.2019.143722.

[49] B.S. Girgis, Y.M. Temerk, M.M. Gadelrab, I.D. Abdullah, X-ray diffraction patterns of activated carbons prepared under various conditions, Carbon Sci. 8 (2007) 95–100, https://doi.org/10.5714/cl.2007.8.2.095.

[50] K. Kumar, R.K. Saxena, V. Kothari, D.K. Suri, N.K. Kaushik, J.N. Bohra, Correlation between adsorption and X-ray diffraction studies on viscose rayon based activated carbon cloth, Carbon N. Y. 35 (1997) 1842–1844, https://doi.org/10.1016/S0008-6223(97)87258-2.

[51] M. Deraman, R. Daik, S. Soltaninejad, N.S.M. Nor, R. Awitdrus, N.F. Farma, N. H. Mamat, M.A.R.Othman Basri, A new empirical equation for estimating specific surface area of supercapacitor carbon electrode from X-ray diffraction, Adv. Mater. Res. 1108 (2015) 1–7, https://doi.org/10.4028/www.scientific.net/AMR.1108.1.

[52] M. Vinayagam, R. Suresh Babu, A. Sivasamy, A.L. Ferreira de Barros, Biomass-derived porous activated carbon from Syzygium cumini fruit shells and Chrysopogon zizanioides roots for high-energy density symmetric supercapacitors, Biomass Bioenergy 143 (2020), 105838, https://doi.org/10.1016/j.biombioe.2020.105838.

[53] A. Gopalakrishnan, S. Badhulika, Gelatinization assisted synthesis of multi-heteroatoms enriched 3D honeycomb-like porous carbon for high-voltage supercapacitor device, J. Energy Storage 43 (2021), 103261.

[54] Y. Liu, Z. Shi, Y. Gao, W. An, Z. Cao, J. Liu, Biomass-swelling assisted synthesis of hierarchical porous carbon fibers for supercapacitor electrodes, ACS Appl. Mater. Interfaces 8 (2016) 28283–28290, https://doi.org/10.1021/acsami.5b11558.

[55] M.F. Hassan, M.A. Sabri, H. Fazal, A. Hafeez, N. Shezad, M. Hussain, Recent trends in activated carbon fibers production from various precursors and applications—a comparative review, J. Anal. Appl. Pyrolysis 145 (2020), 104715, https://doi.org/10.1016/j.jaap.2019.104715.

[56] Z. Song, L. Miao, H. Duan, L. Ruhlmann, Y. Lv, D. Zhu, L. Li, L. Gan, M. Liu, Anionic co-insertion charge storage in dinitrobenzene cathodes for high-performance aqueous zinc–organic batteries, Angew. Chem. Int. Ed. 61 (2022), e202208821.

[57] S. Ghosh, S. Barg, S.M. Jeong, K. Ostrikov, Heteroatom-doped and oxygen-functionalized nanocarbons for high-performance supercapacitors, Adv. Energy Mater. 10 (2020) 1–44, https://doi.org/10.1002/aenm.202001239.

[58] F. Rouquerol, J. Ruoquerol, K. Sing, Adsorption by powders and porous solids: principles, methodology and applications, in: Adsorpt. by Powders Porous Solids, 1999, pp. 1–26.

[59] X. Yang, L. Kong, M. Cao, X. Liu, X. Li, Porous nanosheets-based carbon aerogel derived from sustainable rattan for supercapacitors application, Ind. Crop. Prod. 145 (2020), 112100, https://doi.org/10.1016/j.indcrop.2020.112100.

[60] Y. Guo, T. Wang, D. Wu, Y. Tan, One-step synthesis of in-situ N, S self-doped carbon nanosheets with hierarchical porous structure for high performance supercapacitor and oxygen reduction reaction electrocatalyst, Electrochim. Acta 366 (2021), 137404, https://doi.org/10.1016/j.electacta.2020.137404.

[61] W. Li, C. Chen, H. Wang, P. Li, X. Jiang, J. Yang, J. Liu, Hierarchical porous carbon induced by inherent structure of eggplant as sustainable electrode material for high performance supercapacitor, J. Mater. Res. Technol. 17 (2022) 1540–1552, https://doi.org/10.1016/j.jmrt.2022.01.056.

[62] R.T. Ayinla, J.O. Dennis, H.M. Zaid, Y.K. Sanusi, F. Usman, L.L. Adebayo, A review of technical advances of recent palm bio-waste conversion to activated carbon for energy storage, J. Clean. Prod. 229 (2019) 1427–1442, https://doi.org/10.1016/j.jclepro.2019.04.116.

[63] J. Zhou, W. Yang, B. Jiang, P. Wang, L. Yan, C. Zhang, G. Huang, F. Yang, Y. Li, Intrinsic defect-rich porous carbon nanosheets synthesized from potassium citrate toward advanced supercapacitors and microwave absorption, Carbon N. Y. 183 (2021) 176–186, https://doi.org/10.1016/j.carbon.2021.06.072.

[64] H. Wang, H. Niu, H. Wang, W. Wang, X. Jin, H. Wang, H. Zhou, T. Lin, Micro-meso porous structured carbon nanofibers with ultra-high surface area and large supercapacitor electrode capacitance, J. Power Sources 482 (2021), 228986, https://doi.org/10.1016/j.jpowsour.2020.228986.

[65] E. Taer, A. Afrianda, R. Apriwandi, A.Agustino Taslim, R.Farma Awitdrus, Production of activated carbon electrodes from sago waste and its application for an electrochemical double-layer capacitor, Int. J. Electrochem. Sci. 13 (2018) 10688–10699, https://doi.org/10.20964/2018.11.27.

[66] Y. Zhao, C. Dong, L. Sheng, L. Sheng, Z. Xiao, L. Jiang, X. Li, M. Jiang, J. Shi, Heteroatom-doped pillared porous carbon architectures with ultrafast electron and ion transport capabilities under high mass loadings for high-rate supercapacitors, ACS Sustain. Chem. Eng. 8 (2020) 8664–8674, https://doi.org/10.1021/acssuschemeng.0c01661.

[67] F. Yang, X. Zhang, Y. Yang, S. Hao, L. Cui, Characteristics and supercapacitive performance of nanoporous bamboo leaf-like CuO, Chem. Phys. Lett. 691 (2018) 366–372, https://doi.org/10.1016/j.cplett.2017.11.047.

[68] Atika, R.K. Dutta, Oxygen-rich porous activated carbon from eucalyptus wood as an efficient supercapacitor electrode, Energy Technol. 9 (2021) 1–12, https://doi.org/10.1002/ente.202100463.

[69] K. Liu, J. Xu, Y. Wang, M. Qian, W. Zhao, Y. Zeng, F. Huang, Boron and nitrogen co-doped trimodal-porous wood-derived carbon for boosting capacitive performance, Energy Technol. 8 (2020) 1–9, https://doi.org/10.1002/ente.201900950.

[70] H. Liu, R. Liu, C. Xu, Y. Ren, D. Tang, C. Zhang, F. Li, Y. Wei, R. Zhang, Oxygen–nitrogen–sulfur self-doping hierarchical porous carbon derived from lotus leaves for high-performance supercapacitor electrodes, J. Power Sources 479 (2020), 228799, https://doi.org/10.1016/j.jpowsour.2020.228799.

[71] S. Liu, A. Li, Q. Han, C. Yang, H. Li, H. Xia, F. Ouyang, J. Zhou, X. Liu, Oxygen-directed porous activation of carbon nanospheres for enhanced capacitive energy storage, J. Power Sources 483 (2021), 229223, https://doi.org/10.1016/j.jpowsour.2020.229223.

[72] A. Gopalakrishnan, S. Badhulika, From onion skin waste to multi-heteroatom self-doped highly wrinkled porous carbon nanosheets for high-performance supercapacitor device, J. Energy Storage 38 (2021), 102533, https://doi.org/10.1016/j.est.2021.102533.

[73] N. Sudhan, K. Subramani, M. Karnan, N. Ilayaraja, M. Sathish, Biomass-derived activated porous carbon from rice straw for a high-energy symmetric supercapacitor in aqueous and nonaqueous electrolytes, Energy Fuels 31 (2017) 977–985, https://doi.org/10.1021/acs.energyfuels.6b01829.

[74] Q. Liang, L. Ye, Z.H. Huang, Q. Xu, Y. Bai, F. Kang, Q.H. Yang, A honeycomb-like porous carbon derived from pomelo peel for use in high-performance supercapacitors, Nanoscale 6 (2014) 13831–13837, https://doi.org/10.1039/c4nr04541f.

[75] X. Hao, J. Wang, B. Ding, Y. Wang, Z. Chang, H. Dou, X. Zhang, Bacterial-cellulose-derived interconnected meso-microporous carbon nanofiber networks as binder-free electrodes for high-performance supercapacitors, J. Power Sources 352 (2017) 34–41, https://doi.org/10.1016/j.jpowsour.2017.03.088.

[76] A. Jain, M. Ghosh, M. Krajewski, S. Kurungot, M. Michalska, Biomass-derived activated carbon material from native European deciduous trees as an inexpensive and sustainable energy material for supercapacitor application, J. Energy Storage 34 (2021), 102178, https://doi.org/10.1016/j.est.2020.102178.

[77] N. Yadav, Promila Ritu, S.A. Hashmi, Hierarchical porous carbon derived from eucalyptus-bark as a sustainable electrode for high-performance solid-state supercapacitors, Sustain. Energy Fuels 4 (2020) 1730–1746, https://doi.org/10.1039/c9se00812h.

[78] R. Arunachalam, R.K.V. Prataap, R.Pavul Raj, S. Mohan, J. Vijayakumar, L. Péter, M.Al Ahmad, Pulse electrodeposited RuO2 electrodes for high-performance supercapacitor applications, Surf. Eng. 35 (2019) 103–109, https://doi.org/10.1080/02670844.2018.1426408.

Cassava peel derived self-doped and hierarchical porous carbon as an optimized electrode for the ultra-high energy density of supercapacitor

ORIGINALITY REPORT

12%	1%	2%	11%
SIMILARITY INDEX	INTERNET SOURCES	PUBLICATIONS	STUDENT PAPERS

PRIMARY SOURCES

1	Submitted to Universidad Estadual Paulista Student Paper	1%
2	Submitted to Texas State University- San Marcos Student Paper	<1%
3	Submitted to Tezpur University - CN-173457 Student Paper	<1%
4	revistas.udea.edu.co Internet Source	<1%
5	Submitted to University of Louisiana, Lafayette Student Paper	<1%
6	Submitted to University of Western Ontario Student Paper	<1%
7	Submitted to UC, San Diego Student Paper	<1%
8	Submitted to Universitas Diponegoro Student Paper	<1%

9	Submitted to Unviersidad de Granada Student Paper	<1 %
10	Submitted to Imperial College of Science, Technology and Medicine Student Paper	<1 %
11	Submitted to Queen Mary and Westfield College Student Paper	<1 %
12	Submitted to SASTRA University Student Paper	<1 %
13	Submitted to Chungnam National University Student Paper	<1 %
14	Submitted to Dhaka University of Engineering & Technology Student Paper	<1 %
15	Submitted to Indian Institute of Science Education and Research (IISER) Bhopal Student Paper	<1 %
16	Submitted to Universidade de Évora Student Paper	<1 %
17	Submitted to Universiti Teknikal Malaysia Melaka Student Paper	<1 %
18	Submitted to University of Pretoria Student Paper	<1 %

19	Millán Ponce Modesto. "Estudio de los procesos de polimerización y depolimerización del poli-3-hidroxibutirato (P3HB) en cultivos de Azotobacter vinelandii bajo condiciones controladas de tensión de oxígeno disuelto", TESIUNAM, 2017 Publication	<1 %
20	Submitted to University Der Es Salaam Student Paper	<1 %
21	Submitted to Carnegie Mellon University Student Paper	<1 %
22	Submitted to Queen's University of Belfast Student Paper	<1 %
23	Submitted to Chonnam National University Student Paper	<1 %
24	Submitted to Napier University Student Paper	<1 %
25	Submitted to Universiti Malaysia Sabah Student Paper	<1 %
26	Submitted to Istanbul Aydin University Student Paper	<1 %
27	Colunga Salas Pablo Francisco. "Situación actual de la borreliosis en méxico en la interfase humano-vector-hospedero", TESIUNAM, 2021 Publication	<1 %

28	Submitted to University of Ulster Student Paper	<1%
29	Submitted to University of Newcastle Student Paper	<1%
30	Submitted to Hanoi Metropolitan University Student Paper	<1%
31	Submitted to Jawaharlal Nehru University (JNU) Student Paper	<1%
32	Kota Muninathan, Madhavan Venkata Ramanan. "Enhancement of Sapindus Trifoliatus Biodiesel Production and Performance using Mg-doped CaO Nanocatalyst", Research Square Platform LLC, 2022 Publication	<1%
33	Rivera Medina Martha Judith. "Preparación y caracterización de películas delgadas luminiscentes de ZNS activadas con europio depositadas por la técnica de rocío pirolítico ultrasónico", TESIUNAM, 2016 Publication	<1%
34	Submitted to Campbellsville University Student Paper	<1%
35	Submitted to Federal University of Technology Student Paper	<1%

36	Submitted to Nanyang Technological University Student Paper	<1%
37	Submitted to The University of Manchester Student Paper	<1%
38	Submitted to Anna University Student Paper	<1%
39	Submitted to Kyungpook National University Student Paper	<1%
40	Submitted to Universitat Politècnica de València Student Paper	<1%
41	Submitted to University of Bath Student Paper	<1%
42	Submitted to University of Glasgow Student Paper	<1%
43	Submitted to Boston University Student Paper	<1%
44	Submitted to Mahidol University Student Paper	<1%
45	Submitted to Universidade do Porto Student Paper	<1%
46	Submitted to Alfaisal University Student Paper	<1%

47	Submitted to Babes-Bolyai University Student Paper	<1 %
48	Submitted to Florida A&M University Student Paper	<1 %
49	Submitted to The Robert Gordon University Student Paper	<1 %
50	Submitted to Universiti Malaysia Perlis Student Paper	<1 %
51	Submitted to Universiti Tenaga Nasional Student Paper	<1 %
52	Submitted to University of Birmingham Student Paper	<1 %
53	Submitted to Universiti Malaysia Kelantan Student Paper	<1 %
54	Submitted to University of St Andrews Student Paper	<1 %
55	Submitted to University of Warwick Student Paper	<1 %
56	Ramírez Cruz Gonzalo Ángel. "Dinámica de la presencia de especies invasoras y migratorias y su interacción con especies nativas y residentes en una reserva ecológica inmersa en un ambiente urbano", TESIUNAM, 2019 Publication	<1 %

57	Submitted to University of Surrey Student Paper	<1%
58	www.nlife.jp Internet Source	<1%
59	Martínez Bautista Rubén. "Ensamble y caracterización de media celda de combustible de óxidos sólidos, a base de ceria", TESIUNAM, 2018 Publication	<1%
60	Sánchez Romero Rosa. "Estudio socioecológico del manejo silvopastoril en el bosque tropical seco de la costa centro de Jalisco, México", TESIUNAM, 2020 Publication	<1%

Exclude quotes	Off	Exclude matches	Off
Exclude bibliography	Off		